


## Control of viscous fingering: From the perspective of energy evolution

Hongzhi Ma and Quanzi Yuan \*

*State Key Laboratory of Nonlinear Mechanics, Institute of Mechanics, Chinese Academy of Sciences,  
Beijing 100190, People's Republic of China  
and School of Engineering Science, University of Chinese Academy of Sciences,  
Beijing 100049, People's Republic of China*



(Received 27 September 2020; accepted 11 January 2021; published 1 February 2021)

Improving the ability to control viscous fingering instabilities plays an essential role in a wide variety of scientific and engineering fields. Based on linear stability analysis, we present an energy model characterized by the viscous dissipation rate, which can reflect the evolution process of the fluid-fluid interface, and predictions of control schemes are obtained from the model. One type of scheme is to control the morphological patterns of instability through initial disturbances. Another series of schemes is to control whether the viscous fingering instability is suppressed or continues to develop by different scaling laws of injection rate versus time based on the variational method. Furthermore, a stable and continual forward movement of the interface is achieved by a periodic suppression scheme, which is significant in practical applications. The effectiveness of the energy model and all control schemes are well verified by experiments.

DOI: [10.1103/PhysRevFluids.6.023901](https://doi.org/10.1103/PhysRevFluids.6.023901)

### I. INTRODUCTION

As a typical type of fingering instabilities, viscous fingering (VF) is a phenomenon of fluid-fluid interface instability due to large viscosity ratio. Hele-Shaw cells are the general physical model for studying VF, which can be divided into linear and radial according to different geometry. The instabilities corresponding to these two geometries are called linear VF with an initial planar interface [1–4] and radial VF with an initial circular interface [5–7] respectively. In the fields of energy industry [8,9], microfluidics [10,11], life science, etc., VF plays an important role. For instance, there is VF when HCI passes through gastric mucin [12] as well as VF-like instabilities such as growth of bacterial colonies [13] and spreading of epithelial monolayer tissues [14] in the life science. In turn, because complex behaviors of living systems and fluid instabilities of nonliving systems have similar geometrical morphologies, multiscale fractal-like structures [15] produced by VF can be used to mimic life structures such as lungs, leaf veins, and blood vessels.

Research on the VF instability can be traced back to the 1950s [16,17]. After 70 years, the driving modes of this instability have developed into electric field drive [18], electric field and pressure gradient codrive [19], and so on. However, there is still something unclear about the traditional pressure gradient driving mode. The main theory describing the VF phenomenon is the linear stability analysis first established by Saffman and Taylor. From the perspective of force analysis, linear stability analysis gives a certain amount of state information such as the wave number with the fastest growth rate, but it cannot give more information reflecting the time course of VF. For instance, how will the fluid-fluid interface develop when it is disturbed by an arbitrary single sine wave and what is the specific process of the interface transition between stable and unstable states

---

\*yuanquanzi@lnm.imech.ac.cn

over time? Moreover, VF has evolved into many variants including suspensions of particles [20], non-Newtonian fluids [21,22], nonflat Hele-Shaw cells [23], debonding [24,25] in lifted Hele-Shaw cells, etc. These variants are already new phenomena in which VF instabilities still occur. Needs and challenges raised by the new phenomena require further development of current theories. Hence, we attempt to establish a theoretical model from the perspective of energy evolution, so as to reflect the process of VF more deeply and clearly, and further to explore control schemes of VF instabilities.

Among a mass of practical applications, it is necessary to suppress VF instabilities in some places. During enhanced oil recovery [8,26,27], the finger-shaped interface formed when injected water or supercritical CO<sub>2</sub> displaces oil preferentially reaches production wells, which reduces recovery efficiency greatly. In addition, with the exploitation of nuclear energy and renewable energy such as solar, wind, and geothermal energy, people are faced with the problem of how to store a large amount of energy. One effective solution is to convert the energy into hydrogen, which is then stored underground and retrieved for use when needed. Nevertheless, during displacement of groundwater by hydrogen [9,28,29], VF will result in gas leakage from anticlinal traps, and accelerate gas dissolution owing to increased interface area.

On the other hand, it is required to intensify VF instabilities in some other places. In chemical synthesis in microfluidic devices and miscibility of fluids at low Reynolds numbers, the process of VF is itself a mixing process, so the more severe the instability, the higher the mixing efficiency [10,11]. Besides, one may take advantage of VF to generate dense branched morphologies with fractal dimensions [30–32], which is beneficial to pattern formation [33–35]. Consequently, whether suppression or intensification, control of interfacial instabilities is essential in engineering and design.

There are two main research routes for controlling VF instabilities. One route is to vary flow geometry including replacing rigid walls of Hele-Shaw cells with elastic membranes [36–38], increasing gap thickness with time following  $t^{1/7}$  [39], and changing gap depth linearly along the flow direction [40]. Another route is altering injection rates, which is more convenient to implement in practice than the route mentioned above, including three cases: (1) the rate decreases obeying  $t^{-1/3}$  [41], (2) the rate increases with time in a piecewise-constant manner [42], (3) the rate increases with time in a linear manner [43]. These rate-altering schemes are all aimed at radial VF while there is nearly none for linear VF as far as we are concerned.

This paper considers VF in a linear Hele-Shaw cell. Based on linear stability analysis, an energy model characterized by the viscous dissipation rate is derived and intuitively reflects the time course of instabilities relying on a three-dimensional surface of energy rate. Subsequently, experiments of single sine-wave disturbances are carried out to verify the validity of the energy model. Finally, rate-altering control schemes, of which the critical scaling exponent is  $\alpha_c = -2/3$ , are constructed in the energy model by means of variational method. Comparison with experiments shows that scaling exponents larger than  $-2/3$  leads to unstable fingering growth, while scaling exponents smaller than this critical value result in stable growth. And, it is found that a periodic scheme can achieve a stable and continual forward movement of the fluid-fluid interface. It is hoped that our work could help to understand the physical mechanism behind VF and improve the ability to control VF.

## II. THEORETICAL MODEL

In order to explain the derivations of our energy model in Sec. II B, we first briefly revisit important results of the linear stability analysis of VF in linear Hele-Shaw cell in Sec. II A.

### A. Linear stability analysis

As shown in Fig. 1 the system studied in this paper is a linear Hele-Shaw cell, in which the width direction  $y$  is infinite and the part between  $y = 0$  and  $y = h$  is selected as the object of interest.  $b$  is the gap thickness between two parallel plates. The Hele-Shaw cell is prefilled with fluid 2; then, fluid 1 is injected from the left at a volume flow rate as  $Qbh$ . The average position of the interface

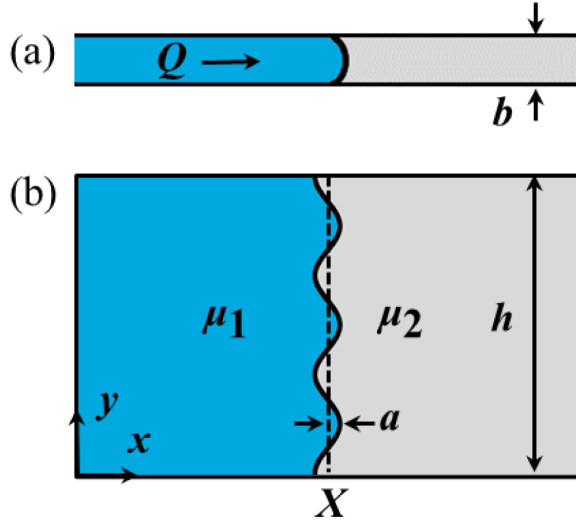


FIG. 1. (a) Side view and (b) top view of the schematic of viscous fingering when one fluid displaces another fluid in a Hele-Shaw cell. The arrow in (a) represents the injection direction of fluid 1.

between two fluids is  $X$  as there is no disturbance. VF instabilities occur at the interface when the dynamic viscosity of fluid 1 is less than that of fluid 2. The velocities of two fluids are controlled by Darcy's law and the continuity equation

$$\begin{aligned} \langle v_j \rangle &= -M_j \nabla p_j \\ \nabla v_j &= 0, \end{aligned} \quad (1)$$

where  $M_j = b^2/12\mu_j$ ,  $\langle v_j \rangle$ ,  $p_j$ ,  $\mu_j$  are the fluid mobility,  $z$ -direction depth-averaged velocity, pressure, and dynamic viscosity, respectively;  $j = 1, 2$  represent the displacing and displaced fluids, respectively.

Let the velocity potential be

$$\phi_j = M_j p_j. \quad (2)$$

As shown in Fig. 1(b), a single-wave-number sine perturbation  $a = Af \cos(2\pi ny/h)$  is imposed at the interface, where  $A$ ,  $f$ ,  $n$  are the amplitude at the initial moment, a variation factor of amplitude over time, and the wave number, respectively. Considering the continuity condition of normal velocity at the interface, the perturbation solution of Eq. (1) is expressed as

$$\phi_j = -Q \left[ x + \left( -1 + \frac{M_j}{M_2} \right) X \right] + (-1)^j \frac{Ahf}{2\pi n} \left[ \exp \left( 2\pi n \frac{x-X}{h} \right) \right]^{(-1)^j-1} \cos \left( 2\pi n \frac{y}{h} \right), \quad (3)$$

where the overdot represents the derivative with respect to time.

Consequently, the growth rate of amplitude as

$$\lambda = \frac{\dot{f}}{f} = \frac{2\pi n}{h(\mu_1 + \mu_2)} \left[ Q(\mu_2 - \mu_1) - \frac{\gamma}{3} \left( \pi n \frac{b}{h} \right)^2 \right] \quad (4)$$

is obtained from the Young-Laplace equation and the fastest-growing wave number as

$$n_m = \sqrt{\frac{(\mu_2 - \mu_1)Q}{\gamma} \frac{h}{\pi b}} \quad (5)$$

is gotten from  $\partial\lambda/\partial n = 0$ , where  $\gamma$  is the interfacial tension.

**B. Energy model**

From Eqs. (1)–(3), the depth-averaged velocity field of this system is

$$\langle v_1 \rangle = \begin{cases} \langle v_{1x} \rangle = Q + \frac{2\pi n}{h} \beta \exp\left(2\pi n \frac{x-X}{h}\right) \cos\left(2\pi n \frac{y}{h}\right) \\ \langle v_{1y} \rangle = -\frac{2\pi n}{h} \beta \exp\left(2\pi n \frac{x-X}{h}\right) \sin\left(2\pi n \frac{y}{h}\right) \end{cases}, \quad (6)$$

$$\langle v_2 \rangle = \begin{cases} \langle v_{2x} \rangle = Q + \frac{2\pi n}{h} \beta \exp\left(-2\pi n \frac{x-X}{h}\right) \cos\left(2\pi n \frac{y}{h}\right) \\ \langle v_{2y} \rangle = \frac{2\pi n}{h} \beta \exp\left(-2\pi n \frac{x-X}{h}\right) \sin\left(2\pi n \frac{y}{h}\right) \end{cases}, \quad (7)$$

where the parameter  $\beta = Ahf/2\pi n$ . Considering the Poiseuille flow with  $z$ -direction distribution, the velocity field becomes

$$v_j = \frac{3}{2} \left[ 1 - \left( \frac{2z}{b} \right)^2 \right] \langle v_j \rangle. \quad (8)$$

Viscous dissipation rate refers to the reduction of mechanical energy caused by dissipation per unit time [44]. For incompressible fluid, the viscous dissipation per unit volume and unit time is in the form of  $\Phi_j = \mu_j (\partial v_i / \partial x_k + \partial v_k / \partial x_i)^2 / 2$ . Substituting Eq. (8) into it, the viscous dissipation rates of the two fluid elements 1 and 2 are, respectively,

$$\Phi_1 = \frac{144\mu_1}{b^4 h^4} \left\{ \begin{aligned} & h^4 z^2 Q^2 + 4\pi n \beta Q h^3 z^2 \exp\left(2\pi n \frac{x-X}{h}\right) \cos\left(2\pi n \frac{y}{h}\right) \\ & + \pi^4 n^4 (b^2 - 4z^2)^2 \beta^2 \exp\left(4\pi n \frac{x-X}{h}\right) + 4\pi^2 n^2 h^2 z^2 \beta^2 \exp\left(4\pi n \frac{x-X}{h}\right) \end{aligned} \right\}, \quad (9)$$

$$\Phi_2 = \frac{144\mu_2}{b^4 h^4} \left\{ \begin{aligned} & h^4 z^2 Q^2 + 4\pi n \beta Q h^3 z^2 \exp\left(-2\pi n \frac{x-X}{h}\right) \cos\left(2\pi n \frac{y}{h}\right) \\ & + \pi^4 n^4 (b^2 - 4z^2)^2 \beta^2 \exp\left(-4\pi n \frac{x-X}{h}\right) + 4\pi^2 n^2 h^2 z^2 \beta^2 \exp\left(-4\pi n \frac{x-X}{h}\right) \end{aligned} \right\}. \quad (10)$$

Integrating the above two expressions under the condition that the perturbation is considered to be a microperturbation, the viscous dissipation rate of the fluid in the range of  $h$  lengths on both sides of the interface is obtained as

$$\begin{aligned} \Phi_{in} &= \iiint_{\Omega_1} \Phi_1 dx dy dz + \iiint_{\Omega_2} \Phi_2 dx dy dz \\ &= (\mu_1 + \mu_2) \left[ \frac{12h^2 Q^2}{b} + \frac{3A^2 f^2 (5h^5 + 8\pi^2 n^2 b^2)}{5\pi n b} + \frac{6A f Q h^2 \sin(2\pi n)}{b\pi^2 n^2} \right]. \end{aligned} \quad (11)$$

The unknown quantity, i.e., the variation factor  $f$  of the disturbance amplitude, can be obtained by integrating the growth rate in Eq. (4):

$$\begin{aligned} f &= \exp(I) \\ I &= \int_0^t \lambda dt. \end{aligned} \quad (12)$$

The forces both at the interface and inside the two-phase fluid are balanced. Consequently, the positive work done by an “injection system” to the fluid through pressure gradient is completely

consumed by the viscous dissipation inside the fluid. Considering the two-phase fluid and the injection system as a whole, the entire system is continuously dissipating energy and the total energy dissipation rate (EDR) is

$$E = -\Phi_{in}. \quad (13)$$

Let the EDR of the undisturbed term be  $E_{up} = -12(\mu_1 + \mu_2)h^2Q^2/b$ ; then, the EDR of the disturbed term is  $E_p = E - E_{up}$ . Extracting the characteristic EDR of perturbation in the form of  $12\pi\gamma^2A^2/b(\mu_1 + \mu_2)$  when  $\gamma$ ,  $b$ , and  $\mu_j$  are constant, then the dimensionless EDR of the disturbed term is

$$E_p^* = E_{pt}^* + E_{pn}^*, \quad (14)$$

where

$$E_{pt}^* = -n \left[ 1 + \frac{8}{5} \left( \frac{\pi nb}{h} \right)^2 \right] \left[ \frac{(\mu_2 - \mu_1)Q}{\gamma} - \frac{1}{3} \left( \frac{\pi nb}{h} \right)^2 \right]^2 \exp(2I), \quad (15)$$

$$E_{pn}^* = -\frac{Qh(\mu_1 + \mu_2)}{\pi^2 n A \gamma} \left[ \frac{(\mu_2 - \mu_1)Q}{\gamma} - \frac{1}{3} \left( \frac{\pi nb}{h} \right)^2 \right] \exp(I) \sin(2\pi n), \quad (16)$$

are the developmental and the fluctuation terms of dimensionless EDR, respectively.

When the injection rate  $Q$  is constant, the values of parameters used in general experiments are  $b = 1$  mm,  $h = 10$  cm,  $Q = 1.86$  mm/s,  $\mu_1 = 1.19$  mPa s,  $\mu_2 = 500$  mPa s, and  $\gamma = 37.65$  mN/m, which are consistent with the values we used in Sec. III A for the sake of comparison with our experiments later. In the linear stage of instability, the initial amplitude of disturbance (0.72 mm used in simulations in Ref. [43]) only changes the fluctuation intensity of EDR, and does not have an essential influence on the paths of interface evolution. However, the initial amplitude cannot be too large, otherwise it does not meet the linear condition. So, after selecting among different values, a moderate-sized initial amplitude of  $A = 0.1b$  is used. Substitute these values above into Eqs. (14)–(16) to draw three-dimensional surfaces of the EDR as shown in Figs. 2(a)–2(c).

The system state (the interfacial wave number and EDR) at any time corresponds to a point on three-dimensional surfaces of EDR, and thus the evolution of system states over a period of time corresponds to a path on three-dimensional surfaces. Time compels the system state to move in the positive direction of the  $t$  axis. At the same time, the EDR is always minimized, which makes the system state tend to stay in the lowest position on three-dimensional surfaces.

Figure 2(b) visualizes a three-dimensional surface of the developmental term, on which, at the zero moment, starting from any point corresponding to a perturbation wave number, EDR will spontaneously decrease with time, and will change in the direction of  $n_m = 5$ . Another three-dimensional surface of the fluctuation term in Fig. 2(c) fluctuates periodically with the wave number, forming multiple potential barriers. The developmental and the fluctuation terms are superimposed to obtain a three-dimensional surface of the total disturbed term as plotted in Fig. 2(a), which both decays in the direction of time and fluctuates in the direction of wave number. This constrains the path starting from any initial moment not to develop in the direction of  $n_m = 5$  with the lowest EDR globally, but to move forward along the potential well with the lowest EDR locally. Thus, with the help of three-dimensional surfaces, the energy model successfully illustrates the evolution of instability over time.

### III. EXPERIMENTS

#### A. Experimental setup

We have improved the existing experimental setup, which is schematically shown in Fig. 3. The low-viscosity fluid (a glycerol aqueous solution, mass fraction: 5.9%,  $\mu_1 = 1.19$  mPa s) and the high-viscosity fluid (silicone oil,  $\mu_2 = 500$  mPa s,  $\gamma = 37.65$  mN/m) are stored in the liquid

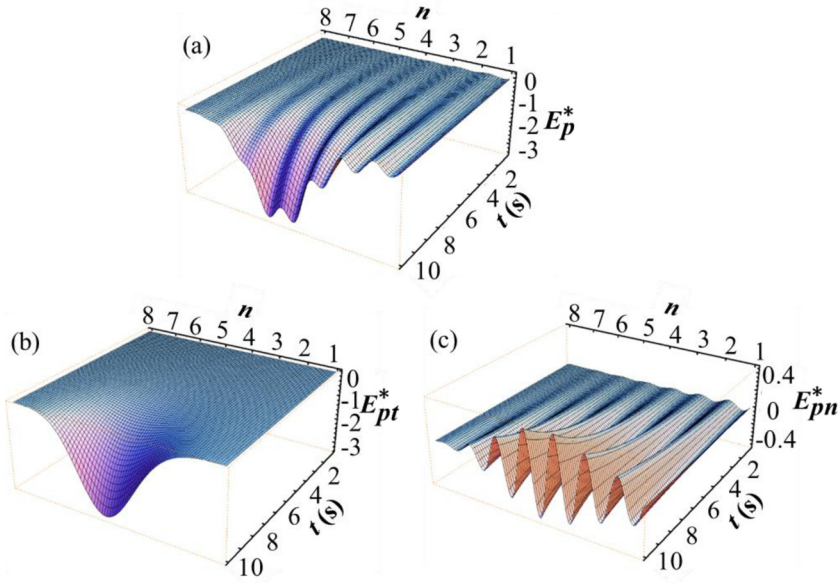


FIG. 2. The theoretically derived three-dimensional surface (a) of the total disturbed term of EDR  $E_p^*$  is the superposition of (b) the developmental term and (c) the fluctuation term.  $n$  and  $t$  represent wave number and time, respectively.

pool and the waste pool, respectively. Through a syringe pump, the low-viscosity fluid is injected ( $Q = 1.86 \text{ mm/s}$ ), then the two-phase fluid is driven to move in a two-dimensional flow channel ( $b = 1 \text{ mm}$ ,  $2h = 20 \text{ cm}$ , closed at  $y = -0.5h$  and  $y = 1.5h$ ; the material of the upper and lower plates is polymethyl methacrylate (PMMA), and the plates' thickness of 2 cm can effectively prevent

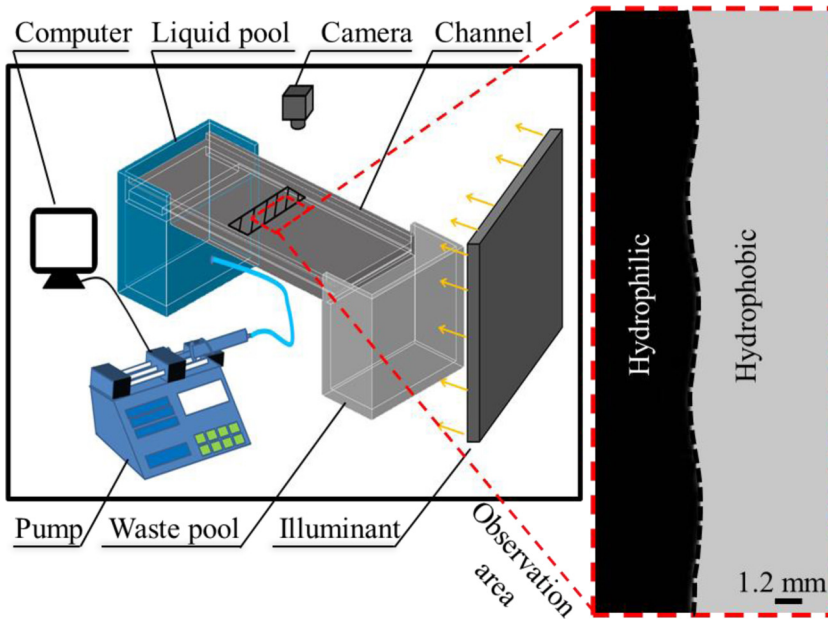


FIG. 3. A schematic of the experimental setup.

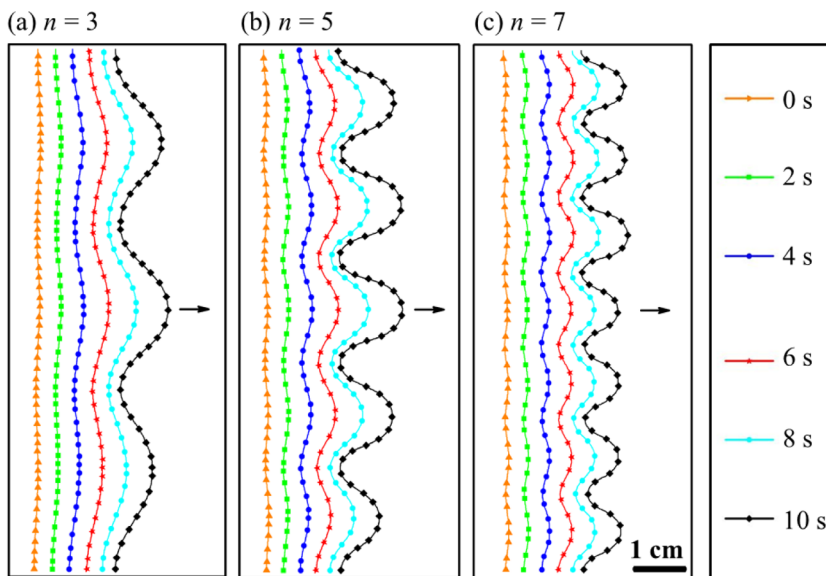


FIG. 4. Snapshots of the evolution of the interface and gradual instability in experiments. The perturbations at the initial moment are in the form of a single sine wave with wave numbers (a)  $n = 3$ , (b)  $n = 5$ , and (c)  $n = 7$ , respectively.  $\Delta t = 2$  s, and the arrow represents the direction of interface movement.

any bending). The movement of the interface between two fluids in the middle area of width  $h$  is recorded with a digital camera (EOS 80D, Canon). In addition, we have developed a set of MATLAB scripts that can communicate with the syringe pump through a computer to achieve variable injection rates of arbitrary functions.

On the right-hand side in Fig. 3, the shape of the interface perturbed ( $A = 0.3b$ ) at the initial moment is illustrated by an enlarged view of the observation area, in which, surface modified by the acrylic UV resin coating, the black region is hydrophilic in the silicone oil environment, while the gray region is hydrophobic without surface modification. A chemical field formed by this difference in properties can exert a predesigned initial perturbation to the interface when the interface is gently adjusted to the position of the coating.

The acrylic UV resin coating used here is a film with a thickness of  $90 \mu\text{m}$ . The film is cut into a rectangle with dimensions of  $20 \text{ cm} \times 1 \text{ cm}$  through an ultraviolet picosecond laser processing system (DL566PU), and the shape of an initial perturbation is cut on one long side of the rectangle according to the function  $a = A \cos(2\pi ny/h)$ . Then the film is closely attached to the lower plate in the flow channel according to the position shown in Fig. 3. In addition, it is worth mentioning that Ref. [45] achieved the control of initial shapes of the air-oil interface in linear Hele-Shaw cells through the gap step.

Among all the values of liquid properties and geometric parameters mentioned above in this section, only the initial disturbance amplitude  $A$  is slightly different from that in theoretical Sec. II B, which will not bring a qualitative difference to the experimental verification. And, unless otherwise specified, these parameter values are still used in subsequent experiments.

### B. Initial disturbances of a single sine wave

Using the above experimental setup, we carry out experiments to verify the energy model. In the experimental results as shown in Fig. 4, the wave numbers of single sine-wave disturbances at the initial moment are designed to be (a)  $n = 3$ , (b)  $n = 5$ , and (c)  $n = 7$ , respectively. From the interface evolution over time, we can find that when the injection rate is constant, the wave

numbers of the interfaces keep their initial values after the initial perturbations become unstable. Wave numbers of 3 and 7 have not evolved towards  $n_m = 5$ , which has the largest growth rate. This is consistent with theoretical descriptions that the interface keeps its own wave number unchanged as it moves forward, and verifies the energy model in Sec. II B. Moreover, the results also indicate that the wave numbers of initial disturbances determine the wave numbers of instability patterns, which provides a method for controlling the instability morphologies.

Another thing worth mentioning is that when  $Q$  is constant, the relationship between EDR and the variation factor of amplitude is  $E_p^* \sim -(f^2 + f)$ , which means that the theoretical response to the amplitude development in experiments is the decrease of EDR.

#### IV. SCHEMES TO CONTROL INSTABILITIES

Control of interfacial instabilities plays a significant role in many practical applications. In some places, it is hoped that either the occurrence of instability can be suppressed, or the interface that has become unstable can be suppressed back to a stable state, while enhanced or sustained instabilities are desired in some other places. Using our energy model, it is possible to construct schemes to control instabilities through variational method.

##### A. Theoretical predictions

Taking changing injection rates as an example,  $\dot{X} = Q$  is the velocity of the unperturbed interface,  $I = [(X - X_0)(\mu_2 - \mu_1) - \gamma(\pi nb/h)^2 t/3]2\pi n/h(\mu_1 + \mu_2)$ , and  $E_{pt}^* = E_{pt}^*(t, X, \dot{X})$  are obtained from Eqs. (4), (12), and (15), where  $X_0 = X(t = 0)$ . A variational approach is employed and the development term  $E_{pt}^*$  is substituted into the Euler-Lagrange equation:

$$\frac{d}{dt} \left( \frac{\partial E_{pt}^*}{\partial \dot{X}} \right) = \frac{\partial E_{pt}^*}{\partial X}. \quad (17)$$

In consideration of the fastest growing wave number  $n_m$  and  $\mu_1 \ll \mu_2$ , Eq. (17) results in an ordinary differential equation  $\ddot{X} = -c_1 \dot{X}^{2.5}$ , namely  $\dot{Q} = -c_1 Q^{2.5}$  for  $Q$ , where  $c_1 = 8/9b\sqrt{\mu_2/\gamma}$ . Substituting the initial condition  $Q(t_0) = Q_0$ , the critical injection rate is solved to be  $Q_c = Q_0[1 + (t - t_0)/t_c]^{-2/3}$ , where  $t_c = (3b/4Q_0)\sqrt{\gamma/Q_0\mu_2}$  is the characteristic time which represents both the timescale of inhibiting instability and the timescale of the linear stage of instability development. Let  $\alpha$  be the scaling exponent; then the form of scaling law of the injection rate is

$$Q \sim (t/t_c)^\alpha. \quad (18)$$

The critical scaling exponent is  $\alpha_c = -2/3$ , and the values on both sides of  $-2/3$  correspond to different rate curves as shown in Fig. 7(d).

The developmental term  $E_{pt}^*$  is used here without considering the fluctuation term  $E_{pn}^*$ , because  $E_{pt}^*$  controls characteristics of the EDR variation in the  $t$  direction while  $E_{pn}^*$  controls that in the  $n$  direction. The determinant of instability is the developmental term. Taking the fluctuation term into account has little effect on stability; instead, it will increase the difficulty of mathematics.

According to different scaling laws, three-dimensional surfaces of  $E_{pt}^*$  are drawn to get Figs. 5(a)–5(c), where the arrows represent lower envelope curves of the curved surfaces, which reflect the lowest trend of EDRs and are also evolution paths of EDRs corresponding to an initial perturbation of wave number  $n = 5$ . After a constant injection time of  $t_0$ , while the scaling exponent goes from small to large, the behaviors of evolution paths in turn are as follows: (c) direct climbing, (b) climbing slowly after lowering briefly, and (a) continuing to lower. The path trend corresponding to the critical scaling exponent of  $\alpha_c = -2/3$  in Fig. 5(b) is reflected in more detail in the contour map of Fig. 5(d), in which the red curves are three contours with the lowest EDR, indicating that the lowest EDR point is after the time  $t_0$ .



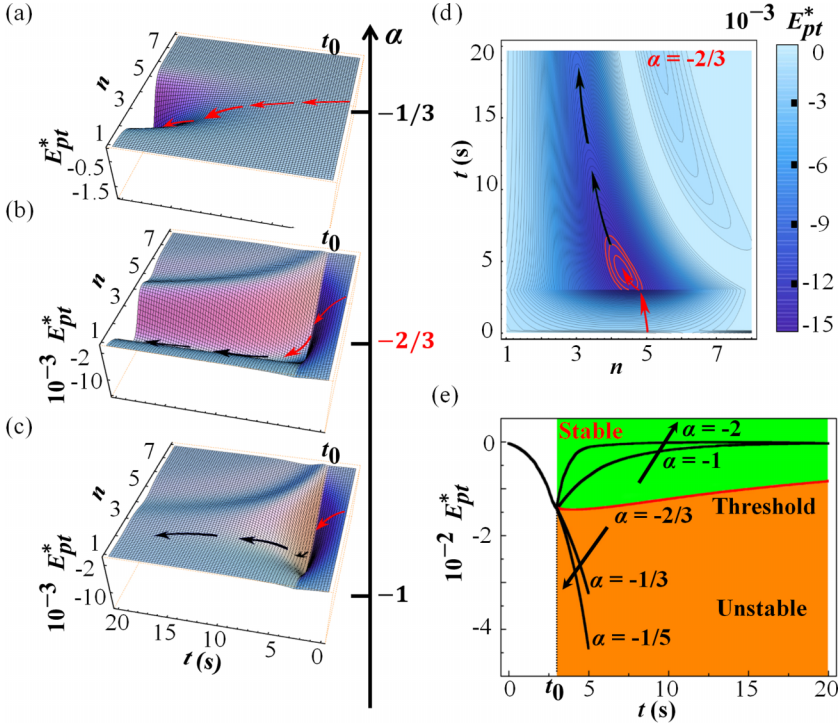


FIG. 5. Evolution paths of EDRs. (a)–(c) Three-dimensional curved surfaces of EDRs, where injection rates are all constant before  $t_0$  moment followed by a decrease. The corresponding scaling exponents  $\alpha$  of injection rates with respect to time are  $-1/3$ ,  $-2/3$ , and  $-1$ , respectively. Arrows represent lower envelope curves of the curved surfaces, among which red arrows indicate a decrease in EDR, and conversely black arrows indicate an increase in EDR. (d) A contour map obtained by projecting the curved surface in (b) onto the  $n-t$  plane, where the color legend on the right-hand side stands for the magnitude of EDR. (e) is gained through projecting the evolution paths in (a)–(c) onto the  $E_{pt}^* - t$  plane.

By means of projecting the evolution paths in Figs. 5(a)–5(c) on the  $E_{pt}^* - t$  plane, the paths corresponding to different scaling laws can be gathered together and are easy to compare with each other as plotted in Fig. 5(e), from which the following points of view can be drawn: (1) when the scaling exponent is less than  $-2/3$ , the EDR is forced to rise, indicating that instability is suppressed; thus, green stands for the stable region; (2) when the scaling exponent is greater than  $-2/3$ , the EDR continues to decrease spontaneously, indicating that the instability continues to develop, so orange represents the unstable region; (3) the scaling exponent  $\alpha_c = -2/3$  is a threshold that divides the development and suppression of instability.

## B. Experimental verifications

Experiments are carried out according to injection rates designed in the theoretical predictions, in which  $t_0 = 3$  s and  $Q_0 = 1.86$  mm/s are parameters for the phase of constant injection. The experimental results are shown in Fig. 6, where injection rates are constant on the left-hand side of the black dashed lines, and decrease according to different scaling laws on the right-hand side. In Figs. 6(a)–6(c), the scaling exponent is less than or equal to  $-2/3$ , and the interfaces that fluctuate due to instability at the constant rate stage gradually become flat with time during the deceleration stage, signifying that interface instabilities have been suppressed. On the other hand, in Figs. 6(d) and 6(e) with scaling exponent greater than  $-2/3$ , the already fluctuating interfaces

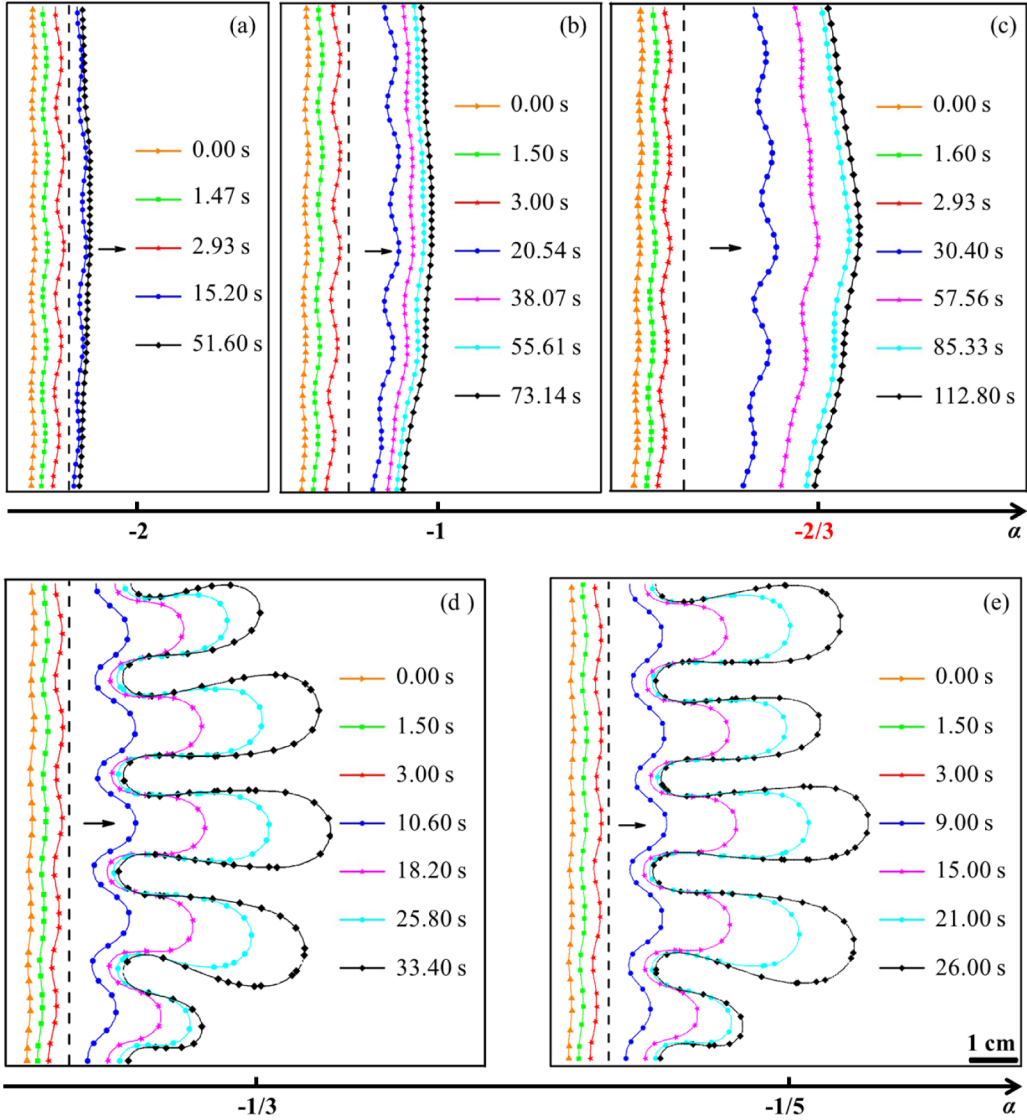


FIG. 6. Experiment. (a)–(e) Five sequences of snapshots of interface movements, in which the scaling exponent  $\alpha$  ranges from  $-2$  to  $-1/5$ , and the arrows represent the direction of interface movements.

will further develop towards instability over time and gradually form “long fingers” during the deceleration stage, meaning that interface instabilities cannot be suppressed. Our purpose here is to study whether fingering continues to develop or is suppressed when it just starts happening. And, these experimental results of controlling instabilities are consistent with theoretical predictions in Sec. IV A.

To further quantify the processes of interface evolution, we identify and extract amplitudes of the intermediate wave in experiments (Fig. 6) as  $A_f$  according to the schematic shown in Fig. 7(a), resulting in Fig. 7(b). Then, a smoothing spline fitting is performed on the amplitude data, and fitting curves are differentiated with respect to time to obtain the growth rate  $\dot{f}$  of the variation factor of amplitude [Fig. 7(c)]. It can be seen that when  $\alpha \leq -2/3$ , after the injection slows down, the growth rates  $\dot{f}$  gradually decrease to negative values, so that amplitudes begin to decay. The amplitudes are

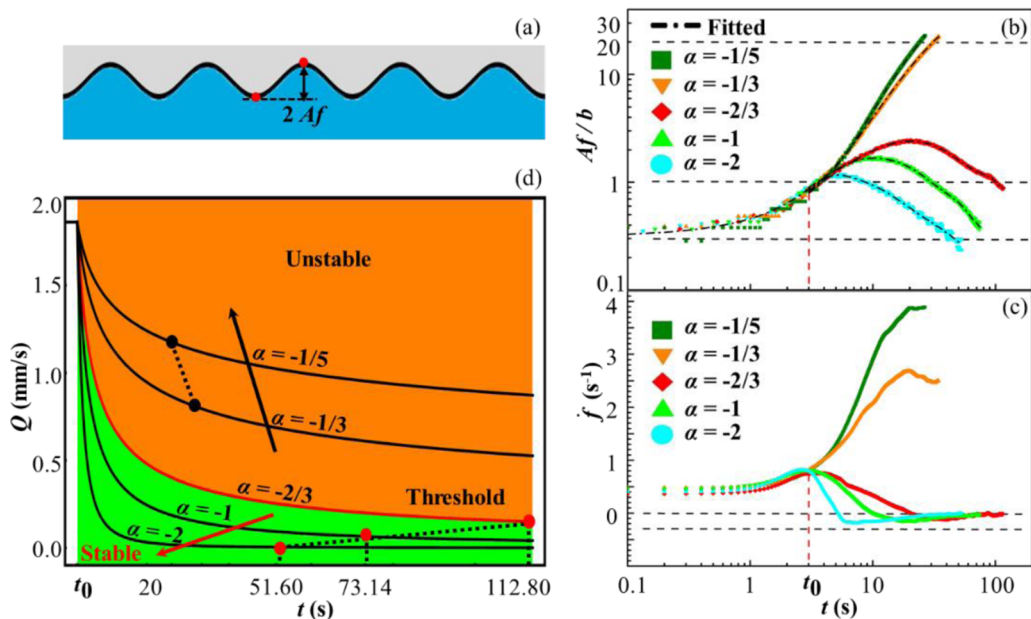


FIG. 7. (a) A schematic of the amplitude  $Af$  of the middle wave in the experiment. (b) Changes in amplitude over time corresponding to Fig. 6. The dashed-dotted lines are the smoothing spline fitting of experimental data, and only the fitting curve of  $\alpha = -1$  is presented when  $t < t_0$  for the sake of clarity. The horizontal and vertical axes are logarithmic. (c) The growth rate  $\dot{f}$  of the variation factor of amplitude. (d) Curves of injection rate vs time for different scaling laws. Orange represents the unstable region where instabilities develop, green represents the stable region where instabilities are suppressed, and the red curve of injection rate represents the boundary between the stable and unstable regions. The red and black dots reflect the last moments of the interface movements in Figs. 6(a)–6(c) and Figs. 6(d) and 6(e), respectively.

all eventually reduced below the thickness  $b$  of the Hele-Shaw cell. At this time, the amplitudes are already small enough, and it can be considered that interfaces become “flat.” As for the interfaces as a whole [Figs. 6(a)–6(c)], there is still a slight bending, which is due to the effect of interfacial tension over a long period of time. When  $\alpha > -2/3$ , the growth rates  $\dot{f}$  increase all the way, and then maintain at high levels, so that amplitudes exceed  $20b$  in a relatively short time. Moreover, from the trend of growth rates, amplitudes will not decay for a considerable time to come. The evolutions of growth rates, interfaces, and amplitudes prove the effectiveness of control schemes with different scaling exponents.

Here, the control of instabilities is considered from the aspect of controlling amplitudes, so changes in wave numbers are not quantitatively analyzed. Intuitively, in experiments (Fig. 6) the wave numbers remained almost unchanged, similar to the cases of constant injection rate (Fig. 4). In EDR [Figs. 5(a)–5(c)], wave numbers decrease with time, which is because the fluctuation term of EDR, which can constrain wave numbers to be nearly constant, is not added for the sake of concision.

Another thing worth noting is that the minimum values of growth rates  $\dot{f}$  for  $\alpha \leq -2/3$  seems to have a limit whose value is about  $-0.2 \text{ s}^{-1}$ . In theory, combine Eqs. (12) and (18) to get

$$\dot{f} = \lambda \exp\left(\int_0^t \lambda dt\right), \quad (19)$$

$$\lambda = \frac{2\pi n}{h(\mu_1 + \mu_2)} \left[ Q_0 \left(1 + \frac{t - t_0}{t_c}\right)^\alpha (\mu_2 - \mu_1) - \frac{\gamma}{3} \left(\pi n \frac{b}{h}\right)^2 \right]. \quad (20)$$

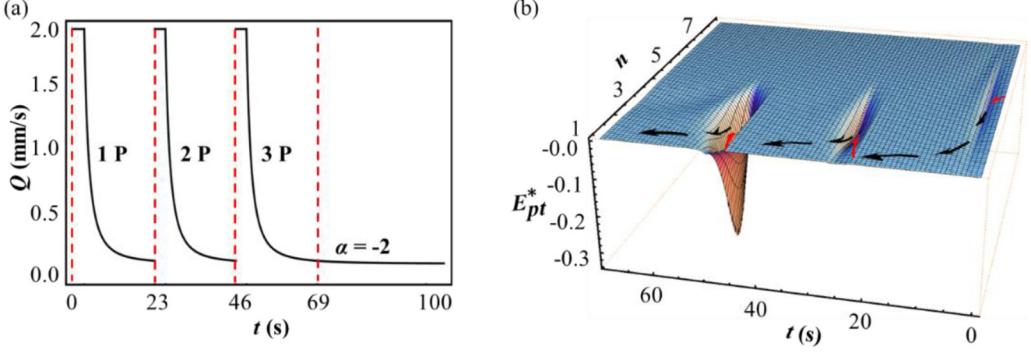


FIG. 8. A periodic suppression scheme (a) and the corresponding EDR surface (b). 1 P, 2 P, and 3 P stand for the first, second, and third periods, respectively. The arrows (the lower envelope curve of the curved surface; red ones decrease, black ones increase) reflect the EDR evolution path starting from wave number  $n = 5$ .

Safely considering  $n$  to be constant of 5 and take the limit  $\alpha \rightarrow -\infty$ , we get

$$\dot{f}_i = \lim_{\alpha \rightarrow -\infty} \dot{f} = -s \exp(-st), \quad t \geq t_0, \quad (21)$$

$$s = \frac{2\pi^3 n^3 b^2 \gamma}{3h^3(\mu_1 + \mu_2)}. \quad (22)$$

At  $t_0$ , there is a minimum value as  $\dot{f}_{i \min} = -0.108 \text{ s}^{-1}$ , which is close to the experimental limit of  $-0.2 \text{ s}^{-1}$ . According to Eq. (21), the later the injection rate begins to decrease, the greater the  $\dot{f}_{i \min}$  and the slower the instabilities are suppressed.

Time information of the experimental results in Fig. 6 is gathered on the curves of injection rate as illustrated in Fig. 7(d), where red dots reflect the moments at which instabilities are suppressed corresponding to Figs. 6(a)–6(c), while black dots reflect the final moments of interface movements in Figs. 6(d) and 6(e). It can be seen that taking  $\alpha_c = -2/3$  as a boundary: (1) the smaller the scaling exponent is, the shorter the time required to achieve the stable state as indicated by the red arrow, thus the faster the suppression; (2) the larger the scaling exponent is, the shorter the time required to arrive at the same degree of instability as implied by the black arrow, thus the more severe the instability.

### C. A periodic control scheme

The rate-varying schemes of suppressing instabilities require that the scaling exponent is not greater than  $-2/3$ , which means that at the same time the interface is suppressed to reach a stable state, the injection rate of the system will tend to zero, making the interface unable to move forward continuously. This limits applications of the suppression schemes in practice. It can be found from red dots in Fig. 7(d) and the final positions of interfaces in Figs. 6(a)–6(c) that among all possible suppression schemes, the scheme of critical scaling exponent  $-2/3$  has the highest injection rate and the largest displacement of interface movement when inhibiting instability, hence to be the best suppression scheme while there is still the problem of limiting interface movement.

Lins and Azaiez [46,47] explored periodic injection rate protocols of sinusoidal functions in radial Hele-Shaw cells, and revealed a resonance effect. To overcome the limitation, we designed a scheme where the injection rate changes periodically over time. Taking three periods as an example, each period starts with a constant rate of 3 s followed by a 20-s deceleration with a scaling exponent of  $-2$ , as shown in Fig. 8(a). After three cycles, enough time continuing to slow down is taken to stabilize the interface. Observing the corresponding evolution path in Fig. 8(b), it is found that due to the existence of the time-integral term  $I$  in EDR [Eq. (15)], the potential wells in three periods

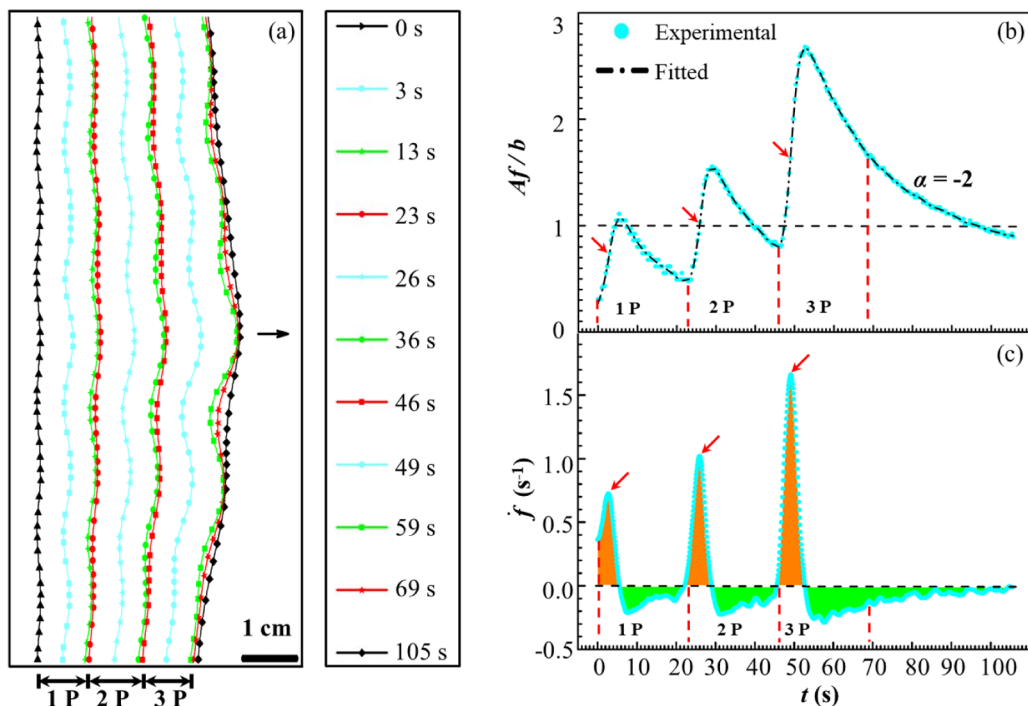


FIG. 9. (a) A continual and stable movement of the fluid-fluid interface realized in the experiment. (b), (c) Changes of the amplitude  $Af$  of the middle wave and the growth rate  $\dot{f}$  with time, respectively. The dashed-dotted line is the smoothing spline fitting of experimental data. Red arrows mark the moments when the injection rate begins to decrease. The areas of regions surrounded by the curve  $\dot{f}$  and the horizontal line  $\dot{f} = 0$  represent the amplitude. The areas of orange (green) regions are positive (negative), representing the amplitude development (decay). In each cycle, the areas of orange and green regions are roughly of equal size, which means that the amplitude after development can be suppressed.

1 P, 2 P, and 3 P deepen in sequence, while the periodic suppression scheme can force the evolution path to climb out of each potential well successfully.

An experiment is performed at the injection rate designed in Fig. 8(a), and the resulting interface evolution process is illustrated in Fig. 9(a). Comparing with Fig. 6(a), it is obvious that the periodic suppression scheme could break the previous restrictions on interface movement, and realize controlling the fluid-fluid interface to move forward stably and continuously, which has important practical significance. Quantitatively, behaviors of the amplitude  $Af$  and the growth rate  $\dot{f}$  are discussed as follows.

The amplitude  $Af$  in Fig. 9(b) increases and decreases periodically with time, and is lower than the thickness  $b$  of flow channel after each decrease. It is worth noting that the value of  $Af$  at the end of each cycle gradually increases, which is due to the existence of the time-integral term  $I$  in  $f$  [Eq. (12)]. Therefore, some additional time is required to stabilize the interface after the 3 P ends.

In Fig. 9(c), the amount of time of constant injection stage is the same for three cycles, but the peak of  $\dot{f}$  increases sequentially owing to the time-integral term  $I$  contained in  $\dot{f}$ . What is more, as can be seen from the red arrows in Figs. 9(b) and 9(c), when the injection rate begins to decrease, the growth rate immediately responds in a decreasing manner while the amplitude does not decay until the growth rate drops to zero. Combined with Fig. 5(c), it is found that EDR also responds immediately to the decrease of injection rate in a manner of climbing, which is because EDR and the growth rate have the following relationship:  $E_{pt}^* \sim -\dot{f}^2$ .

## V. CONCLUSION

In summary, we have explored how to improve the control capability of VF instabilities from two aspects. One aspect is to control patterns of fingering by artificially imposing initial perturbations of the preset wave number. On the other aspect, using rate-altering schemes with different scaling laws, whether the fingering behaviors are suppressed or continue to develop is controlled, and a stable and continual movement of the interface can be achieved through a periodic suppression scheme.

The main innovation of the present work is that an energy model describing the linear VF phenomenon has been developed theoretically based on linear stability analysis. The energy model provides information on the time course of instability, the relationship between initial perturbations and wave numbers of fingering, and so on, which cannot be predicted by linear stability analysis. Therefore, the model gives a train of thought to study VF instabilities from the energy perspective. Here, the theoretical model and rate-altering control schemes based on it have both been verified by experiments.

Our results may be helpful to understand the physical mechanism behind VF in more depth and instruct the prediction, design, and manipulation of stability behaviors of fluid-fluid interface in practical applications. Regarding the possibility of future research, the energy model could be applied to describe a series of variants of the Hele-Shaw cell [20,21,23,24], as well as to seek all kinds of schemes of stability control other than rate-altering ones, such as altering thickness  $b$ , viscosity  $\mu_j$  [48], interfacial tension  $\gamma$ , etc. In addition, the capillary number  $Ca$  dependence [4] can be considered in Eqs. (15) and (16) when  $\mu_1 \ll \mu_2$  and  $Q$  is constant. And, influences of  $Ca$  on the growth rate and EDR are matched, in the sense that  $Ca$  determines the  $n_m$  with the largest growth rate, and EDR also decreases the fastest at  $n_m$ .

## ACKNOWLEDGMENTS

This work was jointly supported by the National Natural Science Foundation of China (NSFC; Grants No. 11722223, No. 12072346, and No. 11672300), the Chinese Academy of Sciences Key Research Program of Frontier Sciences (Grant No. QYZDJ-SSW-JSC019), and the Strategic Priority Research Program of the Chinese Academy of Sciences (Grant No. XDB22040401).

- 
- [1] R. A. Wooding, Growth of fingers at an unstable diffusing interface in a porous medium or Hele-Shaw cell, *J. Fluid Mech.* **39**, 477 (1969).
  - [2] S. P. Gupta, R. A. Greenkorn, and J. E. Varnon, Viscous finger wavelength degeneration in Hele-Shaw models, *Water Resour. Res.* **9**, 1039 (1973).
  - [3] C. W. Park, S. Gorell, and G. M. Homsy, Two-phase displacement in Hele-Shaw cells: Experiments on viscously driven instabilities, *J. Fluid Mech.* **141**, 275 (1984).
  - [4] C. W. Park and G. M. Homsy, Two-phase displacement in Hele Shaw cells: Theory, *J. Fluid Mech.* **139**, 291 (1984).
  - [5] S. D. R. Wilson, A note on the measurement of dynamic contact angles, *J. Colloid Interface Sci.* **51**, 532 (1975).
  - [6] L. Paterson, Radial fingering in a Hele Shaw cell, *J. Fluid Mech.* **113**, 513 (1981).
  - [7] J. Miranda and M. Widom, Radial fingering in a Hele-Shaw cell: A weakly nonlinear analysis, *Physica D* **120**, 315 (1998).
  - [8] S. B. Gorell and G. M. Homsy, A theory of the optimal policy of oil recovery by secondary displacement processes, *SIAM J. Appl. Math.* **43**, 79 (1983).
  - [9] M. Bai, K. Song, Y. Sun, M. He, Y. Li, and J. Sun, An overview of hydrogen underground storage technology and prospects in China, *J. Pet. Sci. Eng.* **124**, 132 (2014).
  - [10] B. Jha, L. Cueto-Felgueroso, and R. Juanes, Fluid Mixing from Viscous Fingering, *Phys. Rev. Lett.* **106**, 194502 (2011).

- [11] B. Jha, L. Cueto-Felgueroso, and R. Juanes, Synergetic Fluid Mixing from Viscous Fingering and Alternating Injection, *Phys. Rev. Lett.* **111**, 144501 (2013).
- [12] K. R. Bhaskar, P. Garik, B. S. Turner, J. D. Bradley, R. Bansil, H. E. Stanley, and J. T. LaMont, Viscous fingering of HCl through gastric mucin, *Nature (London)* **360**, 458 (1992).
- [13] E. Ben-Jacob, O. Schochet, A. Tenenbaum, I. Cohen, A. Czirók, and T. Vicsek, Generic modelling of cooperative growth patterns in bacterial colonies, *Nature (London)* **368**, 46 (1994).
- [14] R. Alert, C. Blanch-Mercader, and J. Casademunt, Active Fingering Instability in Tissue Spreading, *Phys. Rev. Lett.* **122**, 088104 (2019).
- [15] T. ul Islam and P. S. Gandhi, Fabrication of multiscale fractal-like structures by controlling fluid interface instability, *Sci. Rep.* **6**, 37187 (2016).
- [16] P. G. Saffman and G. I. Taylor, The penetration of a fluid into a porous medium or Hele-Shaw cell containing a more viscous liquid, *Proc. R. Soc. London, A* **245**, 312 (1958).
- [17] R. L. Chuoke, P. van Meurs, and C. van der Poel, The instability of slow, immiscible, viscous liquid-liquid displacements in permeable media, *Trans. AIME* **216**, 188 (1959).
- [18] A. A. Fragkopoulos, A. Aizenman, and A. Fernández-Nieves, Charge-induced Saffman-Taylor Instabilities in Toroidal Droplets, *Phys. Rev. Lett.* **118**, 264501 (2017).
- [19] T. Gao, M. Mirzadeh, P. Bai, K. M. Conforti, and M. Z. Bazant, Active control of viscous fingering using electric fields, *Nat. Commun.* **10**, 4002 (2019).
- [20] A. Hooshanginejad, B. C. Druecke, and S. Lee, Stability analysis of a particle band on the fluid–fluid interface, *J. Fluid Mech.* **869**, R2 (2019).
- [21] L. Kondic, M. J. Shelley, and P. Palfy-Muhoray, Non-Newtonian Hele-Shaw flow and the Saffman-Taylor instability, *Phys. Rev. Lett.* **80**, 1433 (1998).
- [22] P. Fast, L. Kondic, M. J. Shelley, and P. Palfy-Muhoray, Pattern formation in non-Newtonian Hele–Shaw flow, *Phys. Fluids* **13**, 1191 (2001).
- [23] L. dos Reis and J. A. Miranda, Controlling fingering instabilities in nonflat Hele-Shaw geometries, *Phys. Rev. E* **84**, 066313 (2011).
- [24] A. Lindner, D. Derks, and M. J. Shelley, Stretch flow of thin layers of Newtonian liquids: Fingering patterns and lifting forces, *Phys. Fluids* **17**, 072107 (2005).
- [25] J. Nase, D. Derks, and A. Lindner, Dynamic evolution of fingering patterns in a lifted Hele–Shaw cell, *Phys. Fluids* **23**, 123101 (2011).
- [26] F. M. Orr and J. J. Taber, Use of carbon dioxide in enhanced oil recovery, *Science* **224**, 563 (1984).
- [27] L. W. Lake, *Enhanced Oil Recovery* (Prentice Hall, Englewood Cliffs, NJ, 1989).
- [28] P. O. Carden and L. Paterson, Physical, chemical and energy aspects of underground hydrogen storage, *Int. J. Hydrog. Energy* **4**, 559 (1979).
- [29] L. Paterson, The implications of fingering in underground hydrogen storage, *Int. J. Hydrog. Energy* **8**, 53 (1983).
- [30] J.-D. Chen, Growth of radial viscous fingers in a Hele-Shaw cell, *J. Fluid Mech.* **201**, 223 (1989).
- [31] O. Praud and H. L. Swinney, Fractal dimension and unscreened angles measured for radial viscous fingering, *Phys. Rev. E* **72**, 011406 (2005).
- [32] J. Mathiesen, I. Procaccia, H. L. Swinney, and M. Thrasher, The universality class of diffusion-limited aggregation and viscous fingering, *Europhys. Lett.* **76**, 257 (2006).
- [33] J. S. Langer, Dendrites, viscous fingers, and the theory of pattern formation, *Science* **243**, 1150 (1989).
- [34] E. Ben-Jacob and P. Garik, The formation of patterns in non-equilibrium growth, *Nature (London)* **343**, 523 (1990).
- [35] J. Casademunt, Viscous fingering as a paradigm of interfacial pattern formation: Recent results and new challenges, *Chaos* **14**, 809 (2004).
- [36] D. Pihler-Puzović, R. Périllat, M. Russell, A. Juel, and M. Heil, Modelling the suppression of viscous fingering in elastic-walled Hele-Shaw cells, *J. Fluid Mech.* **731**, 162 (2013).
- [37] L. Ducloué, A. L. Hazel, D. Pihler-Puzović, and A. Juel, Viscous fingering and dendritic growth under an elastic membrane, *J. Fluid Mech.* **826**, R2 (2017).
- [38] D. Pihler-Puzović, G. G. Peng, J. R. Lister, M. Heil, and A. Juel, Viscous fingering in a radial elastic-walled Hele-Shaw cell, *J. Fluid Mech.* **849**, 163 (2018).

- [39] Z. Zheng, H. Kim, and H. A. Stone, Controlling viscous fingering using time-dependent strategies, *Phys. Rev. Lett.* **115**, 174501 (2015).
- [40] T. T. Al-Housseiny, P. A. Tsai, and H. A. Stone, Control of interfacial instabilities using flow geometry, *Nat. Phys.* **8**, 747 (2012).
- [41] S. Li, J. S. Lowengrub, J. Fontana, and P. Palffy-Muhoray, Control of Viscous Fingering Patterns in a Radial Hele-Shaw Cell, *Phys. Rev. Lett.* **102**, 174501 (2009).
- [42] E. O. Dias, F. Parisio, and J. A. Miranda, Suppression of viscous fluid fingering: A piecewise-constant injection process, *Phys. Rev. E* **82**, 067301 (2010).
- [43] E. O. Dias, E. Alvarez-Lacalle, M. S. Carvalho, and J. A. Miranda, Minimization of Viscous Fluid Fingering: A Variational Scheme for Optimal Flow Rates, *Phys. Rev. Lett.* **109**, 144502 (2012).
- [44] L. D. Landau and E. M. Lifshitz, *Fluid Mechanics* (Pergamon, New York, 1987).
- [45] E. Álvarez-Lacalle, J. Ortín, and J. Casademunt, Nonlinear Saffman-Taylor Instability, *Phys. Rev. Lett.* **92**, 054501 (2004).
- [46] T. F. Lins and J. Azaiez, Flow instabilities of time-dependent injection schemes in immiscible displacements, *Can. J. Chem. Eng.* **94**, 2061 (2016).
- [47] T. F. Lins and J. Azaiez, Resonance-like dynamics in radial cyclic injection flows of immiscible fluids in homogeneous porous media, *J. Fluid Mech.* **819**, 713 (2017).
- [48] T. H. Beeson-Jones and A. W. Woods, Control of viscous instability by variation of injection rate in a fluid with time-dependent rheology, *J. Fluid Mech.* **829**, 214 (2017).